A&A 390, 649–665 (2002)
DOI: 10.1051/0004-6361:20020424

Astronomy & Astrophysics

The physical structure of Magellanic Cloud H II regions⋆

I. Dataset

R. Vermeij[1], F. Damour[2], J. M. van der Hulst[1], and J-.P. Baluteau[2]

[1] Kapteyn Astronomical Institute, PO Box 800, 9700 AV Groningen, The Netherlands
[2] Laboratoire d'Astrophysique de Marseille, CNRS & Université de Provence, BP 8, 13376, Marseille Cedex 12, France

Received 26 October 2001 / Accepted 19 March 2002

Abstract. We present infrared and optical spectroscopic data for 11 H II regions and one Supernova Remnant in the Large and Small Magellanic Cloud. The infrared data have been obtained with the Short Wavelength Spectrometer and Long Wavelength Spectrometer on board the *Infrared Space Observatory* as part of a Guaranteed Time Program on H II regions in Local Group Galaxies. Aim of this project is to give a new and improved analysis of the physical structure of the sample H II regions by combining as much spectral data as possible. A detailed account is given here of the reduction process, and the quality and reliability of the presented fluxes are discussed.

Key words. ISM: lines and bands – H II regions – Magellanic Clouds

1. Introduction

With a plethora of emission lines, from the far ultraviolet all the way to the far infrared, H II regions are a very rich source of spectral information. The huge amount of information contained in the emission lines makes these regions ideally suited for investigating the properties of the local gas-phase interstellar medium (ISM). In principle, it is possible to deduce many of the important characteristics of an H II region from its spectrum.

Among such characteristics are the temperature and density of the electron gas, which can be derived from taking ratios of line fluxes. Well known examples of these are the often employed optical [O III] 5007 Å/4363 Å and [S II] 6717 Å/6730 Å line ratios for the electron temperature and density, respectively. Ratios from spectral lines emitted by different ionic species of the same element constrain the ionization structure inside the H II region. The ionization structure throughout the region reflects the hardness and density of the local radiation field which is a signature of the number and the mass of the major ionizing sources in the H II region. Given a set of electron temperatures and densities, the chemical composition of the gas can be derived from the spectral lines. The abundances thus determined provide clues for the local nucleosynthetic and star-formation history.

Send offprint requests to: R. Vermeij,
e-mail: ronald@astro.rug.nl

⋆ Based on observations with ISO, an ESA project with instruments funded by ESA Member States (especially the PI countries: France, Germany, The Netherlands and the UK) and with the participation of ISAS and NASA.

The analysis of an H II region in terms of the physical structure, stellar content and chemical composition is, however, not without difficulties. The derivation of the physical structure is often limited to the electron temperature and density as found with the "classical" ratios of lines from O^{++} and S^{+}, but by limiting the analysis to these lines, one is actually probing only a part of the total emitting volume of the H II region. This is the result of the stratified nature of the ion distribution within the region. The electron properties found are taken to be representative of the entire nebula, but the existence of density variations and temperature gradients throughout the nebula is not ruled out (the t^2 problem, Peimbert 1967). Gradients and fluctuations in the temperature structure are immediately reflected in the abundances one derives. The abundances are underestimated because of the tendency of temperature fluctuations to bias the temperatures found towards higher values.

The accurate determination of elemental abundances is also hampered by the limited number of ionization stages one can observe for a particular element. For many astrophysically important elements, one often has to make corrections for unseen ionization stages using Ionization Correction Factors (ICFs) in order to derive the total elemental abundance. Many prescriptions for these ICFs have appeared over the last thirty years, either based on coincidences in ionization potentials of various ions (Peimbert & Costero 1969) or on photoionization models (e.g. Grandi & Hawley 1978; Mathis & Rosa 1991). The most difficult element in this respect proved to be sulfur (Natta et al. 1980; Garnett 1989).

Many different diagnostics have been proposed for constraining the effective temperature of the ionizing source of

an H II region. Helium recombination line diagnostics like He I 5875/Hβ are robust but insensitive for T_* higher than 39 000 K (Kennicutt et al. 2000). Single-element forbidden-line diagnostics, like [O III] 5007/Hβ and [Ne III] 3869/Hβ, as well as composite diagnostics, like the η' parameter (Vilchez & Pagel 1988), are also often used. These diagnostics, however, can be sensitive to abundance effects and variations in ionization parameter, especially in spatially resolved nebulae.

To address the problems described above, one needs to use as many spectral lines as possible. By extending the data base from the optical into other spectral regions, such as the infrared, many of the problems can at least be alleviated. The inclusion of more spectral lines makes it possible to derive electron temperatures and densities for more different ions, giving a better coverage of the temperature profile of the nebula. A larger spectral coverage gives us access to more different, otherwise unobservable, ionic species. This makes a direct calculation of the elemental abundance possible without having to resort to ICFs. It also puts more constraints on the ionization structure of the nebula and, therefore, on the nature of the ionizing sources.

For this purpose a large set of new optical and infrared spectroscopic data has been obtained of several bright H II regions in the Magellanic Clouds. The infrared spectra were taken with the *Short Wavelength Spectrometer* (SWS) and *Long Wavelength Spectrometer* (LWS) on board the *Infrared Space Observatory* (ISO, Kessler et al. 1996), as part of a comprehensive ISO Guaranteed Time Program on H II regions in Local Group Galaxies.

The Magellanic Clouds form excellent targets for such studies. With their small distance of 55 kpc (LMC, e.g. Feast 1999) and 65 kpc (SMC, e.g. Kovács 2000), star formation and star-forming regions can be studied in considerable detail, down to the scale of individual stars. Given their high elevation above the Galactic plane, the problem of extinction towards the Magellanic Clouds is less acute than for Galactic H II regions. The study of Galactic H II regions is often limited to the local neighbourhood because of the extinction in the Galactic plane, whereas in the Magellanic Clouds H II regions can be studied on a galaxy wide scale.

In this first of a series of papers, the data are presented. The data set comprises optical driftscan spectra, as well as infrared spectra obtained with the *Infrared Space Observatory* (ISO). The layout of the paper is as follows. Section 2 gives an overview of the objects in the sample and their environment, Sect. 3 gives a detailed account of the reduction of the optical and infrared spectra, and Sect. 4 discusses the quality and reliability of the spectral data presented. The analysis will be deferred to subsequent papers.

2. Sample objects

The selection of the sample objects had to be done with special consideration for the instruments used to observe them, and the use of the ISO satellite had in this respect the most serious impact on our choice of objects. The three main selection criteria for most of the objects in the sample were that they are bright enough to be detectable with ISO, that the geometry is relatively simple, and that the objects are small enough to fit into the ISO-SWS apertures.

Consequently, many of the objects in the sample are bright, highly excited compact blobs (HEBs), of which several have been discovered in the Magellanic Clouds in the last two decades (e.g. Heydari-Malayeri & Testor 1985). These HEBs are usually only a few arcseconds across, can have a rather large dust content (N88A, Kurt et al. 1999) and are small enough to be ionized by only a few massive stars (N81, Heydari-Malayeri et al. 1999c). These HEBs are thought to be the first step in the evolution from an ultracompact H II region towards more extended structures.

The objects observed in this study are given in Table 1 together with the ISO-SWS/LWS pointing coordinates and observation dates. The distribution of the sample H II regions across the Magellanic Clouds can be seen in Fig. 1. A short description of the sample objects, highlighting some of their features, is given below.

2.1. LMC: 30 Doradus

The giant H II region 30 Doradus (N157A) is the most conspicuous object in the Large Magellanic Cloud. Extending about 15′ across the sky, the object is the closest extragalactic giant H II Region. This makes 30 Dor very interesting and the nebula has therefore been the object of many different studies.

The morphology of 30 Dor is very complex, with filaments, bubbles and shells. A thorough kinematic study by Chu & Kennicutt (1994) revealed the presence of networks of high-velocity expanding shells in the inner parts of 30 Doradus. Hot bubbles inside the nebula make 30 Dor a strong diffuse X-ray emitter (e.g. Wang 1999).

Spectrophotometric studies of the region have been performed by e.g. Rosa & Mathis (1987) and Mathis et al. (1985). The spectra, taken at various locations, not only in the inner core of 30 Dor but also in the more diffuse outer parts, have shown the nebula to be chemically homogeneous. The ionization structure of the inner part of 30 Doradus has been investigated using narrow-band WFPC2 images in the Hα, [O III] 5007 Å and the [S II] (6717+6731) Å lines (Scowen et al. 1998).

Studies of the stellar content of 30 Doradus have shown the nebula to be incredibly rich in massive stars (e.g. Parker & Garmany 1993; Hunter et al. 1995). Within the massive star cluster R136 at the core of 30 Doradus, about 39 O3 stars have been found, of which some are supergiants (Massey & Hunter 1998). At least five distinct epochs of consecutive star formation have been identified in 30 Doradus (Walborn & Blades 1997), of which the youngest is still ongoing. The detection of water maser activity near R136 betrays the presence of recently formed stars (Whiteoak et al. 1983; Van Loon & Zijlstra 2001).

In this work, the pointings in 30 Doradus were chosen in a roughly semi-circular pattern centered on the massive central cluster R 136 (see Fig. 2, upper left).

Table 1. The objects contained in the sample. Given are the coordinates of the ISO SWS and LWS pointings. The designations, except for 30 Doradus, are those of Henize (1956).

Object	SWS Coordinates (J2000.0)			LWS Coordinates (J2000.0)		
	RA (h m s)	δ (^{o} $'$ $''$)	Date	RA (h m s)	δ (^{o} $'$ $''$)	Date
N66	0 59 03.7	−72 10 39.9	01-Apr.-1996	0 59 08.0	−72 10 26	01-Apr.-1996
N81	1 09 13.6	−73 11 41.1	14-May-1996	1 09 09.1	−73 12 07	22-Apr.-1996
N88A	1 24 08.1	−73 09 02.5	14-May-1996	1 24 09.4	−73 09 16	22-Apr.-1996
N79A	4 51 47.4	−69 23 47.6	10-Sep.-1996	4 51 49.3	−69 24 36	29-Apr.-1996
N4A	4 52 08.4	−66 55 23.4	29-Apr.-1996	4 52 06.4	−66 55 27	29-Apr.-1996
N83B	4 54 25.2	−69 10 59.8	14-May-1996	4 54 25.2	−69 10 59	01-Nov.-1997
N11A	4 57 16.2	−66 23 18.3	22-Apr.-1996	4 56 48.3	−66 24 11	17-Jul.-1997
N159-5	5 40 02.4	−69 44 33.4	10-Jul.-1996	5 40 04.2	−69 44 42	06-May-1996
N157B	5 37 51.6	−69 10 23.1	14-May-1996	5 37 51.8	−69 10 22	29-Apr.-1996
30 Dor#1	5 38 33.5	−69 06 27.1	05-Dec.-1997	5 38 33.5	−69 06 27	29-Apr.-1996
30 Dor#2	5 38 35.5	−69 05 41.2	13-Apr.-1996	5 38 43.8	−69 05 17	29-Apr.-1996
30 Dor#3	5 38 46.0	−69 05 07.9	06-May-1996	5 38 45.8	−69 05 11	29-Apr.-1996
30 Dor#4	5 38 54.2	−69 05 15.3	05-Aug.-1997	5 38 54.2	−69 05 11	29-Apr.-1996
N160A1	5 39 43.3	−69 38 51.4	10-Jul.-1996	5 39 44.2	−69 38 42	06-May-1996
N160A2	5 39 46.1	−69 38 36.6	10-Jul.-1996	5 39 44.2	−69 38 42	06-May-1996

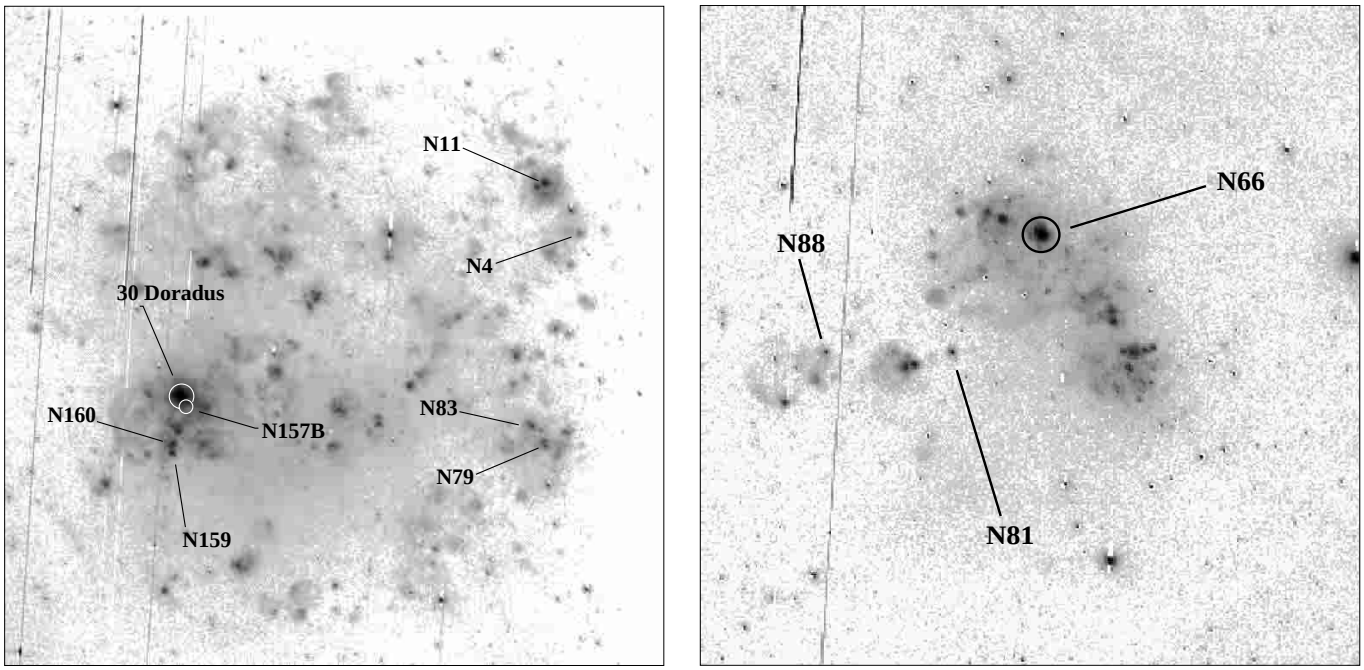

Fig. 1. The Magellanic Clouds in Hα. The LMC is left and the SMC is right. Indicated are the H II regions in the sample. North is up and East is left. The images were obtained with the Parking Lot Camera (Kennicutt et al. 1995; Bothun & Thompson 1988).

2.2. LMC: N4A

The object N4A is located a few arcminutes southwest from N11, and is the brighter of the two parts making up N4. The N4 region has been studied in detail by Heydari-Malayeri & Lecavalier des Etangs (1994). Their study of the morphology of N4A shows the presence of a bright compact structure embedded in fainter nebulosity extending towards the west (see Fig. 2, lower right). Associated with N4A is a molecular complex of which a sheet is located in front of the H II region. In a recent study of N4 with ISOCAM, the presence of emission from Polycyclic Aromatic Hydrocarbons (PAHs) and Very Small Grains (VSGs) was detected (Contursi et al. 1998).

2.3. LMC: N11A

Being the second largest H II region in the LMC after 30 Doradus, N11 lies quite isolated at about 4^o from the LMC bar. The region consists of several parts (N11 A-L,

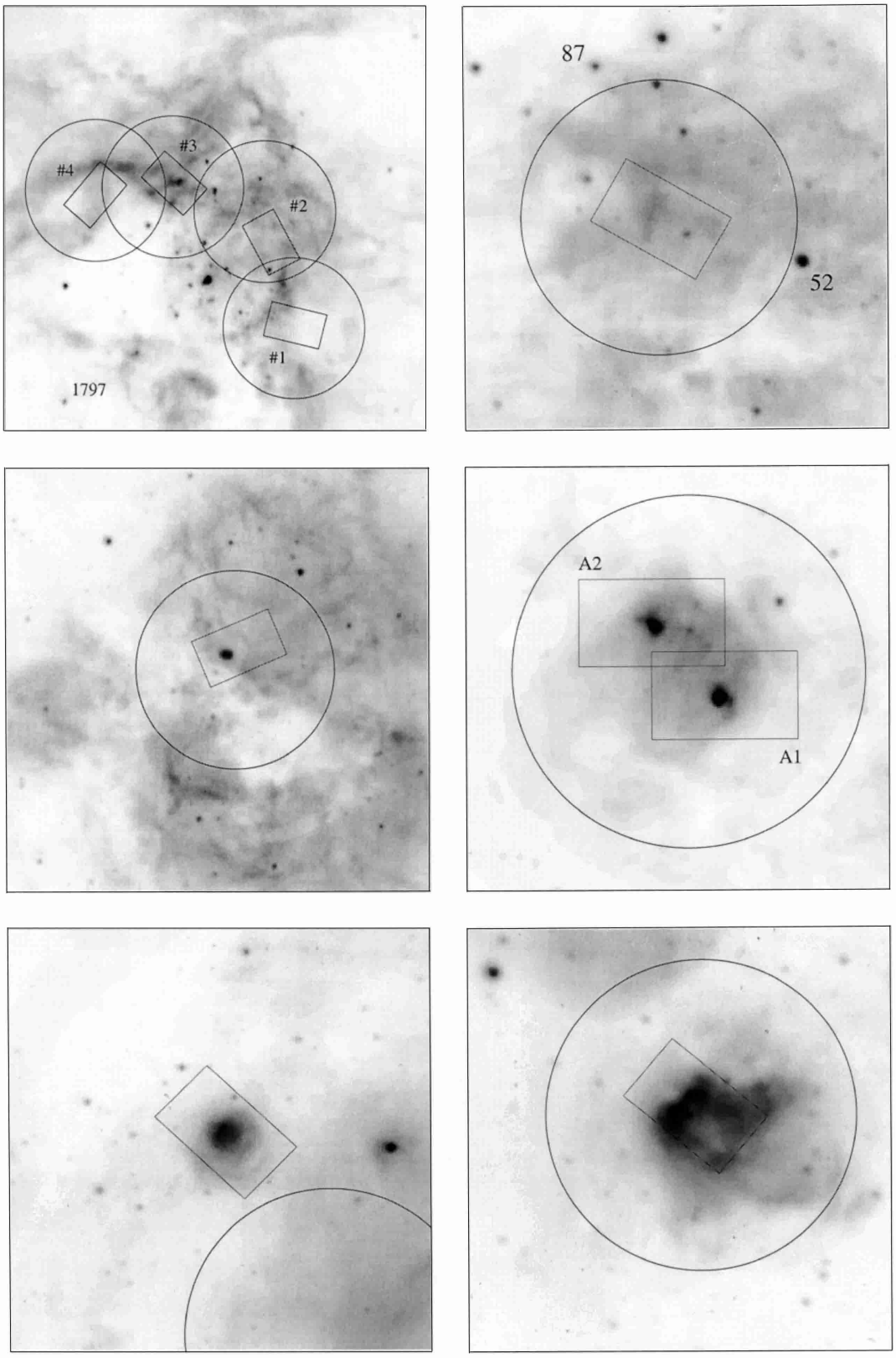

Fig. 2. The LMC objects 30 Doradus (*upper left*), N157B (*upper right*), N159-5 (*middle left*), N160A (*middle right*), N11A (*lower left*) and N4A (*lower right*) in Hα. Shown are the ISO-SWS and ISO-LWS pointings in these objects. The SWS aperture plotted is $20'' \times 33''$ (band 4). The star 1797 in 30 Doradus is from Parker (1993). The stars 52 and 87 in N157B are from Shield & Testor (1992). The white circle shows the position of the X-ray source in N157B. North is up and East is left.

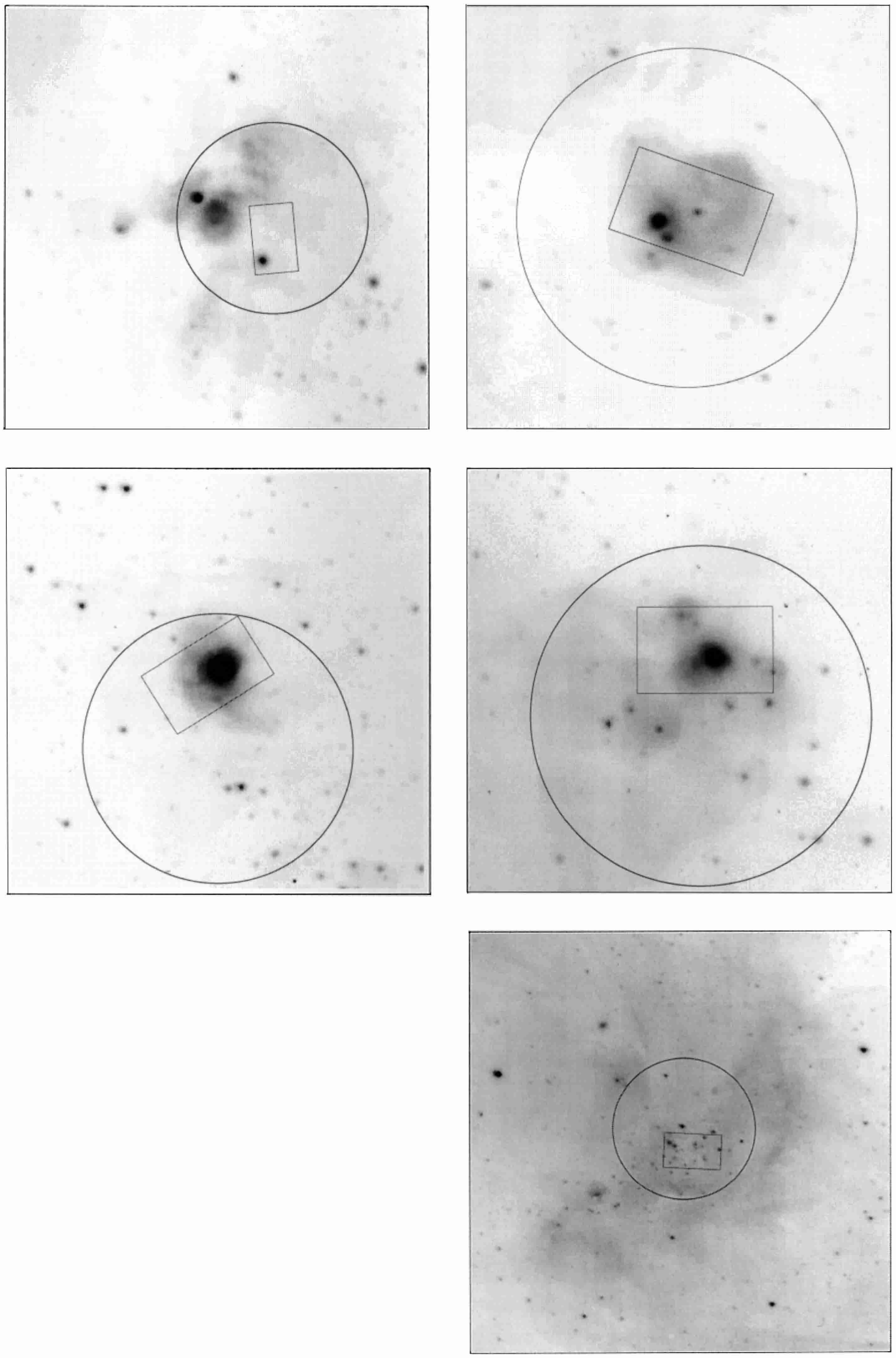

Fig. 3. The LMC objects N79A (*upper left*) and N83B (*upper right*) and the SMC objects N81 (*middle left*), N88A (*middle right*) and N66 (*lower right*) in Hα. Shown are the ISO-SWS and ISO-LWS pointings in these objects. The SWS aperture plotted is $20'' \times 33''$ (band 4). North is up and East is left.

Table 2. The log of the optical observations made in December 1995 and December 1996 at the ESO 1.52 meter telescope.

Observing date	Detector	Grating	Spectral Range	Slit width	Spatial res.	Spectral res.
13/16 Dec. 1995	Ford Aerospace 2048L 15 μm pixels	Grating #2 300 gr mm^{-1}	2880 Å–10 550 Å	1.″7	0.″81 pix^{-1}	3.8 Å pix^{-1}
2/5 Dec. 1996	Loral/Lesser #39 15 μm pixels	Grating #5 900 gr mm^{-1}	3455 Å–11 150 Å	1.″7	0.″81 pix^{-1}	3.8 Å pix^{-1}
		Grating #25 400 gr mm^{-1}	3977 Å–9780 Å			2.8 Å pix^{-1}

Henize 1956), of which N11B is the most prominent. Many rich stellar associations are located in the complex, like LH9 and LH10 (Lucke & Hodge 1970). The sample object N11A (Fig. 2, lower left), a blob of ∼12″ in diameter, is located 1′ east from N11B. The blob is highly excited, showing an [O III]/Hβ ratio in excess of 4 (Heydari-Malayeri & Testor 1983, present work), and is not heavily extincted. A study by Rosado et al. (1996) shows no evidence of disturbed kinematics inside N11A. An HST study of N11A revealed the presence of a tight cluster of stars in the center of the object (Heydari-Malayeri et al. 2001b).

2.4. LMC: N79A and N83B

The H II regions N79 and N83 in the LMC (Fig. 3, upper left and right, respectively) both lie in the western part of the bar. With only the occasional appearance in larger samples for chemical abundance studies (e.g. Pagel et al. 1978), not much attention has been paid to either of these objects. A study of N83B by Heydari-Malayeri et al. (1990) has shown the presence of a very compact blob at the eastern part of the nebula (N83B-1). The morphological study of N83B has been extended using HST (Heydari-Malayeri et al. 2001a), resulting in two new compact blobs being added to the collection (N83B-2 and N83B-3). Both N83B-1 and N83B-2 are clearly visible in the upper right panel of Fig. 3.

2.5. LMC: N157B

The object N157B, lying 6′ south-west from 30 Doradus, is an interesting mix of an H II region and a supernova remnant (SNR). The complex was first recognized to contain an SNR through its Crab-like radio spectrum (Le Marne 1968; Mills et al. 1978), which was later confirmed by others (e.g. Dickel et al. 1994). The discovery of a bright X-ray source at this position by Long & Helfand (1979) established the nature of the object. An optical counterpart in [S II] emission showing signs of shock enhancement was detected by Danziger et al. (1981). It was on this optical counterpart that ISO was pointed (see Fig. 2, upper right). The discovery of an X-ray pulsar with a period of only 16 ms by Marshall et al. (1998) has further strengthened the picture of N157B as a Crab-like SNR.

2.6. LMC: N159-5 and N160A

The H II regions N159 and N160, together with N158, form a nice chain of H II regions extending southwards from 30 Doradus. The regions lie approximately 30′ south from 30 Dor and are very complex. The N160 region is subdivided into two pairs of H II nebulosity, N160 B/C and N160 A/D. The two HEBs observed in this work (N160A1 and A2) are embedded within the component N160A, and clearly stand out in Hα images (see Fig. 2, center right). The H II region N159 roughly consists of two parts, a triangular shaped part (N159A) and a very complex H II structure at the east arching all the way to the north. The object N159-5 is located 6′ north-east of N159A (see Fig. 2, center left). High-resolution HST images of the blob show it to have a "butterfly" like morphology (Heydari-Malayeri et al. 1999b). The HEBs in N160A and N159-5 have about the same angular size, 6″ for N159-5 and ∼4″ for N160A1/A2. Both N159-5 and N160A1 are very highly excited, showing a very high [O III]/Hβ ratio of about 8, with N160A2 only slightly less. Locally, the extinction seen towards the objects is very high, with $A_{\mathrm{H}\beta} = 1.7$ mag for N160A1 and as much as 2.9 mag for N159-5. Much of this extinction is internal, due to the presence of dust in the objects. In a recent HST study of N160A, the two blobs have been resolved and their stellar content determined (Heydari-Malayeri et al. 2002). The CO content of N159 and N160 has been studied by Johansson et al. (1998) as part of the ESO-SEST key programme.

2.7. SMC: N66

The SMC object N66 (NGC 346) is a giant H II region containing about 40 O stars (Massey et al. 1989). As can be seen in the lower right panel of Fig. 3, the region has two distinct components. The first component is a semi-circular nebula showing a wealth of filaments and ridges, while the second component, lying somewhat northeast at the center of the circle, is formed by an isolated H II region known as N66A.

The region has been studied extensively in many wavelength regimes. In the optical, spectroscopic work has been done by e.g. Dufour & Harlow (1977) and Pagel et al. (1978). In a study by Taisheng et al. (1991), a SNR and SNR candidate have been discovered in N66 by using Hα images and radio

data at four frequencies. More recently, the nebula has been observed in the mid-infrared with ISOCAM, complemented by CO(2-1) and H_2 data (Contursi et al. 2000; Rubio et al. 2000). In their work, a detailed study is given of the photodissociation region associated with N66. The presence of PAHs has also been detected. In this work, the ISO satellite was pointed at a position halfway the two main components of N66 (see Fig. 3, lower right).

2.8. SMC: N81 and N88A

The compact SMC H II regions N81 and N88 have been studied by e.g. Testor & Pakull (1985) and Heydari-Malayeri et al. (1988). The large scale morphology of the two objects is reasonably simple. In Hα, N81 shows up as a round object embedded, slightly off-center, in diffuse emission (Fig. 3, center left). The object N88 is composed of four main components forming a roughly triangular shape. The dominant component N88A is a very compact blob of about 4″ in diameter (Fig. 3, center right).

In recent times, both objects have been revisited by Heydari-Malayeri et al. (1999a,c) and Kurt et al. (1999) using the HST. The HST study of N81 revealed a small cluster of stars inside the core of the nebula, with the main exciting sources being two deeply embedded stars only 0.″27 apart. For N88A, the main exciting star could not be identified, which is due to the uncommonly high extinction. Both N81 and N88A show complex structures inside their cores, with dark lanes and bright and dark globules.

3. Data

3.1. Optical data

The optical spectra were secured during two observing runs in December 1995 and December 1996. The observations were carried out with the Boller & Chivens Spectrograph on the ESO 1.52 meter telescope. The instrumental setup in these two runs is given in Table 2. In all cases, the detector was windowed down to 300 × 2048 pixels, giving a slit length of 4.′1. In the second part of the December 1996 run, the grating was changed, which split the spectra in two sets, differing in wavelength range.

Of every H II region in our sample, longslit spectra and several driftscan spectra were taken. The longslit spectra were taken at intervals of 4–5″ in the direction perpendicular to the slit so as to cover the whole object. The orientation of the slit was chosen such that the effects of differential refraction were minimized. The driftscan spectra scan areas ranging from 10″ to 60″, depending on scan speed and integration time, and are used to facilitate the combination of ISO and optical data. These driftscan spectra were obtained holding the slit in a fixed North-South direction. Unless stated otherwise, the reduction process described in this section is the same for both the longslit and the driftscan spectra.

The reduction of the optical spectra was done with the *Image Reduction and Analysis Facility* (IRAF) V2.11. The reduction involved bias subtraction, flatfielding using dome flats, and cosmic ray removal. A slit illumination function was created from sky flats to correct for illumination gradients in the dome flats along the spatial direction of the slit. These gradients, though, amounted to only a few percent going from one end of the slit to the other. Several Helium-Argon lamp exposures were made during every night for the wavelength calibration of the spectra. The Helium-Argon exposures were also used to correct for a slight misalignment of the slit with the dispersion lines of the detector.

For the flux calibration of the spectra, a response function of the total setup was derived using the combined spectra from the standard stars Feige 24, L 745-46A and G 99-37 (Oke 1974). The uncertainty in the response function, and hence in the flux calibration, was determined by overplotting the different "sub" response functions as derived from the separate standard star exposures. The scatter in the combined "sub" response functions as a function of wavelength was then determined. This scatter translated into an uncertainty in the flux calibration varying from 3% in the yellow, central part of the spectrum, to 5% in the red and blue parts at the ends. From the combined "sub" response functions a master response function was derived. The 2D-spectra were then flux calibrated. A correction for atmospheric extinction was made with a standard extinction curve for the site using the airmass in mid-observation. Given the short exposure times of the spectra, the change in the airmass during the observation was negligible.

The background emission was subtracted from the 2D-spectra by fitting a constant function to every dispersion line. To this end, windows were placed along the slit where no nebular emission was present. In some of the spectra, however, the emission was seen to extend all across the slit, particularly in Hα and [O III] 5007 Å. In these cases, two "versions" of the same spectrum were created, one with and one without the background emission removed. This procedure was necessary because of the multitude of nightsky lines in the far red which would otherwise make the identification of the nebular lines difficult.

From the spectra thus reduced a 1D-spectrum was extracted. For the stationary longslit spectra, the number of 1D-spectra extracted and their placing across the slit depend highly on the source under consideration. We therefore defer their discussion to future papers on the separate objects. As far as the driftscan spectra are concerned, the appropriate width and placing of the extraction window for every separate object was derived from the projection of the ISO-SWS band 4 aperture (20″ × 33″) on the slit. Only for the object N159-5 the extraction window was made smaller to tightly fit the knot seen in the center panel of Fig. 2, this to increase the S/N ratio of the spectrum. Decreasing the width of the extraction window to match the projection of the other three (smaller) apertures did not change the derived 1D-spectra significantly.

Fluxes were derived from the 1D-spectra with the SPLOT package. The flux of each line in the spectra was measured several times by fitting Gaussian profiles to the lines as well as by simple pixel integration. These measurements were repeated at least eight times for every line in order to get an estimate of the uncertainties in the line flux due to noise and continuum fitting. For most of the lines the profile was adequately decribed by a Gaussian, but for some of the stronger lines sometimes a

small blue wing was seen. In such cases, the flux derived from the pixel integration was adopted, but the difference between the fluxes derived in the two different ways amounted to only a few percent.

In the case of a spectrum from which it was impossible to subtract the background emission, the line fitting procedure was a bit different. For those lines which did not extend all across the slit, the background subtracted version of the 1D-spectrum was used to derive the fluxes. These lines included the ones blue-wards from Hβ and red-wards from Hα. The lines extending all across the slit were measured in both versions of the 1D-spectrum. The difference in the fluxes derived for those lines was treated as an extra uncertainty.

The line fluxes were corrected for extinction using the Balmer-decrement Hα/Hβ. The only exception here was for some of the spectra of SMC-N81 for which the Hα line was sometimes saturated and Hδ/Hβ had to be used instead. For the unreddened decrements, the Baker & Menzel (1938) Case B values from Storey & Hummer (1995) were taken for T_e = 10 000 Kelvin and n_e = 100 cm^{-3}. The correction was applied taking the extinction curve towards the Magellanic Clouds as parameterized by Howarth (1983), with the usual relation

$$\log(I_\lambda/I_\beta) = \log(F_\lambda/F_\beta) + C(\mathrm{H}_\beta) f_\lambda, \quad (1)$$

with I_λ/I_β and F_λ/F_β the dereddened and reddened fluxes relative to Hβ respectively, f_λ the extinction curve, and $C(\mathrm{H}_\beta)$ the reddening parameter derived from the decrement Hα/Hβ. The amount of extinction in the driftscan spectra is generally low. Assuming an R_V of 3.1, the values for A_V range from ~ 0.1 mag for SMC-N66 to as high as 1.7 mag for the LMC object N159-5.

The line fluxes of a representative sub-sample of the driftscan spectra of the program objects are given in Tables 3 and 4. For all the objects, the spectrum covering the wavelength range from 3400 Å to 10 000 Å is given. For LMC-N83B, LMC-N11A and the pointings in 30 Doradus, however, only driftscan spectra covering the wavelength range from 4000 Å to 9800 Å were available. The error in the fluxes as given in the tables is due to uncertainties in the flux calibration, noise and uncertainties arising from the continuum fitting and background subtraction. The error due to uncertainties in the applied reddening correction is not included, but a typical error for $E_{\beta-\alpha}$ resulting from the uncertainty in the Hα/Hβ decrement is in the order of 0.03 mag. An extra source of uncertainty exists in the fluxes redward from 8000 Å which is a spectral region that can be heavily affected by absorption from atmospheric water. This absorption was clearly present in the standard star exposures and in the objects with a strong continuum. The absorption was not "divided" out of the spectra, but an attempt was made to derive the extra uncertainty in the flux arising from this problem (see Sect. 4.2).

3.2. Infrared data

3.2.1. Short Wavelength Spectrometer

The infrared data obtained with the Short Wavelength Spectrometer (SWS, de Graauw et al. 1996) on board ISO consist of separate line scans (AOT2, covering wavelength ranges from 0.02 to 0.6 μm), AOT6 scans (30 Doradus#1, covering wavelength ranges from 0.22 to 1.7 μm for wavelenghts shorter than 7.0 μm, and from 5.1 to 15 μm for longer wavelengths), and one archival full-grating scan (AOT1 speed 4, 30 Doradus #3). The observations were carried out during the revolutions 136–298 and 519–750. The total spectral coverage of the SWS instrument ranges from 2.4 μm to 45.2 μm. This range is roughly divided into 4 sub-ranges or bands associated with 4 separate detector blocks of 12 detectors each. Each band has its own aperture that increases in size with increasing wavelength. The positions of the band 4 ISO-SWS aperture (20″× 33″) on the sky are shown in Figs. 2 and 3. The SWS AOT2 data were reduced using version 6.0 of the Standard Product Generation pipeline as implemented in Interactive Analysis (IA^3). The AOT6 and AOT1 data were processed with version 8.7. A recalibration of the AOT2 data with pipeline version 8.7 did not change the reduction results from version 6.0, so the first ones were retained. In all cases, the reduction process started at the *Standard Processed Data* (SPD) level.

The reduction of every SPD involved the steps of a zeroth order correction for memory effects, dark current subtraction, response calibration, flux calibration, and a correction for the velocity of the ISO spacecraft in the line of sight towards the object. Special attention was paid to the dark current subtraction step where, when possible, a correction was made for variations in the dark current during a scan. The absence of a continuum in most of the scans made this not too difficult. After the dark current subtraction, the separate up and down scans were checked for symmetry. Finally, bad detectors were removed from the SPD and an *Auto Analysis Result* (AAR) was extracted. The AAR was then flatfielded, sigma clipped to remove spurious points from the scans and rebinned to the default resolution for the particular observing template (3000 for AOT2/AOT6 and 2000 for AOT1 speed 4). This was done for the up and down scans separately, as well as for the combined data.

Fluxes were derived from the AAR by fitting Gaussians to the line profiles using the line-fitting routines within the *ISO Spectral Analysis Package* (ISAP). The fluxes were independently checked with self-developed line-fitting software. In all cases, both flux measurements agreed well. The fluxes derived with the ISAP routines from the combined up and down scans are given in Tables 5 and 6. The fluxes have not been corrected for possible extinction. The highest Brα/Brβ ratio found in our SWS spectra is 2.18 ± 0.32, which is comparable with the Storey & Hummer (1995) Case B value of 1.76 for T_e = 10 000 Kelvin and n_e = 100 cm^{-3}. For some of our objects no estimate of the possible extinction could be made because of the absence of suitable hydrogen recombination lines. The uncertainties in the line fluxes arise mainly from noise, uncertainties in the flux calibration and from the differences in the fluxes as measured from the separate up and down AARs. For most of the objects, the main contributor to the error in the flux is the uncertainty in the flux calibration, which can be as high as 30% for the band 4 lines.

Table 3. The optical fluxes for the LMC objects N160A1, N160A2, N159-5, N157B and the four pointings in 30 Doradus. The first and second column give the wavelength and identification of the lines, respectively. The fluxes are given relative to Hβ (×100). Given in the last row is the reddening $E_{\beta-\alpha}$ in magnitudes. The flux uncertainties are coded as follows: A < 5%, 5% ≤ B < 7.5%, 7.5% ≤ C < 10%, 10% ≤ D < 12.5%, 12.5% ≤ E < 15%, F ≥ 15%.

λ (Å)	Identifier	N160A1		N160A2		N159-5		N157B		30 Dor#1		30 Dor#2		30 Dor#3		30 Dor#4	
		I_λ/I_β	Err	I_λ/I_β	Err	I_λ/I_β	Err	I_λ/I_β	Err	I_λ/I_β	Err	I_λ/I_β	Err	I_λ/I_β	Err	I_λ/I_β	Err
3727	[O II]	165.5	C	164.6	C	246.0	C	223.0	B	–	–	–	–	–	–	–	–
3869	[Ne III]	29.4	B	26.5	C	29.5	E	19.9	D	–	–	–	–	–	–	–	–
3888	Hζ	17.4	C	16.5	C	17.3	E	15.8	D	–	–	–	–	–	–	–	–
3968	[Ne III]	23.6	B	22.2	C	25.2	F	21.3	E	–	–	–	–	–	–	–	–
4101	Hδ	24.7	B	24.2	B	24.6	F	23.3	C	24.1	B	23.0	A	24.9	A	27.3	B
4340	Hγ	44.4	B	44.1	B	47.0	D	42.4	C	50.5	A	48.9	A	49.3	A	52.6	B
4363	[O III]	2.4	D	1.8	E	–	–	4.8	F	4.8	B	3.8	C	3.8	B	3.7	E
4471	He I	3.8	C	3.6	D	–	–	3.5	F	4.2	C	3.7	D	4.3	B	5.4	E
4711	[Ar IV]	–	–	–	–	–	–	–	–	–	–	–	–	0.88	E	–	–
4861	Hβ	100.0	A	100.0	A	100.0	B	100.0	B	100.0	A	100.0	A	100.0	A	100.0	A
4959	[O III]	139.9	A	126.5	A	120.0	B	108.0	B	189.0	A	167.0	C	168.0	A	151.0	A
5007	[O III]	423.6	A	382.1	A	368.0	B	324.0	B	566.0	A	502.0	C	497.0	A	457.0	A
5200	[N I]	–	–	0.49	F	–	–	–	–	–	–	–	–	–	–	–	–
5270	[Fe III]	–	–	–	–	–	–	–	–	0.28	F	–	–	0.26	F	–	–
5517	[Cl III]	0.45	E	0.41	F	–	–	–	–	–	–	0.55	F	0.56	D	–	–
5537	[Cl III]	0.31	F	0.25	F	–	–	–	–	–	–	0.44	F	0.37	D	–	–
5754	[N II]	0.34	F	–	–	–	–	–	–	–	–	–	–	–	–	–	–
5875	He I	12.1	A	11.7	A	12.8	C	11.7	B	11.7	B	13.1	A	12.7	A	12.1	A
6302	[O I]	1.60	B	1.27	C	2.7	F	5.5	C	0.50	E	–	–	0.59	C	1.2	C
6312	[S III]	1.43	B	1.44	C	1.3	F	1.6	C	1.7	C	1.7	F	1.7	B	1.7	C
6362	[O I]	0.71	F	–	–	1.0	F	2.2	F	–	–	–	–	0.29	F	0.68	F
6563	Hα	286.0	A	286.0	A	286.0	B	286.0	B	286.0	A	286.0	A	286.0	A	286.0	A
6585	[N II]	18.7	B	18.3	B	21.0	B	22.2	C	5.2	B	4.7	B	7.9	A	12.9	A
6678	He I	3.3	B	3.2	B	3.4	C	3.8	D	3.3	B	3.3	B	3.6	A	3.2	B
6717	[S II]	12.7	C	11.7	C	18.1	B	29.1	B	3.7	B	5.1	B	4.3	A	8.6	A
6730	[S II]	10.1	C	9.3	C	14.3	B	24.5	B	3.2	B	4.1	B	4.1	A	7.3	A
7065	He I	3.2	B	3.3	B	4.5	C	2.4	E	3.5	B	3.2	B	3.7	A	2.5	B
7137	[Ar III]	11.9	A	11.2	A	12.4	B	10.5	B	11.5	A	11.3	A	12.8	A	11.4	A
7281	He I	0.61	E†	0.59	E†	–	–	–	–	0.46	E†	0.59	E†	0.60	C†	0.53	E†
7320	[O II]	2.6	B†	2.5	B†	3.5	C†	–	–	1.3	C†	1.2	B†	1.7	B†	1.9	B†
7330	[O II]	2.0	B†	2.0	B†	2.7	C†	–	–	1.2	C†	1.0	B†	1.4	B†	1.6	B†
7450	[Fe II] (?)	3.0	C†	2.8	C†	2.4	F†	5.0	F†	–	–	–	–	0.27	F†	–	–
7726	He I	0.57	D	0.45	E	–	–	–	–	0.35	F	–	–	0.37	E	–	–
7751	[Ar III]	3.1	B	2.8	B	3.0	D	–	–	2.9	B	2.9	C	3.3	B	2.7	B
8750	P 12	1.34	D‡	1.3	D‡	2.0	F‡	–	–	1.2	E‡	1.1	D‡	1.3	C‡	1.4	D‡
8862	P 11	2.10	D‡	2.0	C‡	2.4	F‡	–	–	1.6	D‡	1.5	D‡	1.8	C‡	1.6	E‡
9015	P 10	2.05	D‡	2.1	D‡	3.3	F‡	–	–	1.7	F‡	1.8	C‡	1.9	B‡	1.7	D‡
9069	[S III]	37.9	A‡	35.3	A‡	42.6	B‡	35.6	B‡	28.8	A‡	27.0	A‡	32.7	A‡	29.9	A‡
9229	P 9	3.53	B‡	3.4	C‡	4.1	F‡	–	–	3.4	C‡	3.1	C‡	3.8	B‡	3.1	C‡
9532	[S III]	87.1	A‡	82.2	A‡	91.6	B‡	85.8	B‡	79.4	A‡	–	–	97.5	A‡	85.3	A‡
	$E_{\beta-\alpha}$	0.27		0.30		0.59		0.25		0.40		0.35		0.33		0.59	

† These lines sit in an absorption feature near 7200 Å.

‡ The fluxes are affected by telluric absorption. The extra uncertainty arising from this is not included here.

3.2.2. Long Wavelength Spectrometer

The Long Wavelength Spectrometer (LWS, Clegg et al. 1996) on board ISO was used in AOT1 mode to get full grating scan spectra covering the wavelength range from 43 μm to 196 μm. Over this spectral range, the resolving power varies from 140 to 330. The total spectral range covered is split into two sets of five parts each, a Short Wavelength part (SW, 43–93 μm) and a Long Wavelength part (LW, 84–196 μm). Both the SW and LW

Table 4. The same as in Table 3 but then for the LMC objects N11A, N83B, N79A and N4A, and for the SMC objects N88A, N66 and N81.

λ (Å)	Identifier	N11A		N83B		N79A		N4A		N88A		N66		N81	
		I_λ/I_β	Err	I_λ/I_β	Err	I_λ/I_β	Err	I_λ/I_β	Err	I_λ/I_β	Err	I_λ/I_β	Err	I_λ/I_β	Err
3727	[O II]	–	–	–	–	233.0	B	152.2	B	95.6	B	116.9	C	137.0	B
3869	[Ne III]	–	–	–	–	17.7	C	28.0	B	53.6	B	34.1	C	46.0	C
3888	Hζ	–	–	–	–	14.7	C	18.4	C	11.4	C	15.3	E	15.0	D
3968	[Ne III]	–	–	–	–	18.9	C	23.9	B	29.1	C	26.1	F	27.6	B
4101	Hδ	25.9	C	24.5	B	23.4	C	24.7	B	24.7	C	19.7	D	25.4	B
4340	Hγ	52.9	B	54.5	A	41.5	B	44.7	B	44.4	B	40.9	C	45.6	B
4363	[O III]	2.9	F	2.5	F	2.4	F	2.6	F	12.0	C	5.6	F	7.4	B
4471	He I	4.6	C	4.0	E	3.6	E	3.9	D	3.6	E	3.1	F	3.8	D
4711	[Ar IV]	–	–	–	–	–	–	–	–	–	–	–	–	–	–
4861	Hβ	100.0	A	100.0	A	100.0	B	100.0	A	100.0	A	100.0	B	100.0	A
4959	[O III]	128.0	A	92.1	A	101.0	A	142.0	A	222.0	A	156.0	B	175.0	A
5007	[O III]	387.0	A	277.0	A	306.0	A	430.0	A	672.0	A	469.0	B	528.0	A
5200	[N I]	–	–	–	–	–	–	–	–	–	–	–	–	0.4	F
5270	[Fe III]	–	–	–	–	–	–	–	–	–	–	–	–	–	–
5517	[Cl III]	–	–	–	–	–	–	–	–	–	–	–	–	–	–
5537	[Cl III]	–	–	–	–	–	–	–	–	–	–	–	–	–	–
5754	[N II]	–	–	–	–	–	–	0.41	F	–	–	–	–	–	–
5875	He I	12.3	B	11.4	A	11.4	A	12.4	A	12.9	B	11.0	C	10.9	B
6302	[O I]	1.7	D	1.3	D	1.8	C	1.2	C	1.6	C	2.3	E	1.1	C
6312	[S III]	1.5	D	1.4	C	1.3	C	1.5	C	1.6	C	1.8	E	1.6	C
6362	[O I]	–	–	–	–	0.76	F	–	–	–	–	1.4	F	–	–
6563	Hα	286.0	A	286.0	A	286.0	A	286.0	A	286.0	A	286.0	B	–	–
6585	[N II]	17.0	C	22.7	A	23.8	A	13.3	A	5.3	B	6.1	C	5.5	B
6678	He I	3.3	C	3.2	B	3.1	C	3.3	B	2.9	B	3.1	D	2.5	B
6717	[S II]	11.3	E	14.4	C	15.1	A	9.1	A	5.2	B	10.1	B	6.9	B
6730	[S II]	9.3	E	11.8	B	12.5	A	6.9	A	4.5	B	7.0	C	5.2	B
7065	He I	3.2	E	3.8	B	3.9	C	2.6	B	9.3	A	2.9	F	2.7	B
7137	[Ar III]	11.5	B	10.2	A	10.6	B	11.4	A	10.7	A	8.3	C	8.3	A
7281	He I	–	–	–	–	0.74	F†	0.68	F†	0.87	E†	–	–	0.6	F†
7320	[O II]	4.8	C†	4.0	B†	4.1	B†	2.2	C†	2.9	B†	2.1	E†	2.5	C†
7330	[O II]	3.8	C†	3.5	B†	3.3	B†	1.8	C†	2.2	B†	2.0	F†	1.9	C†
7450	[Fe II] (?)	–	–	–	–	5.9	C†	3.4	C†	1.7	F†	3.6	F†	–	–
7726	He I	–	–	–	–	–	–	0.66	E	0.6	F	–	–	1.2	D
7751	[Ar III]	3.3	D	2.7	C	2.7	C	2.9	B	2.2	D	–	–	2.0	C
8750	P 12	–	–	1.5	F‡	1.8	D‡	1.1	E‡	1.8	E‡	–	–	1.2	F‡
8862	P 11	–	–	1.7	F‡	2.7	F‡	1.9	E‡	1.7	E‡	–	–	1.5	F‡
9015	P 10	–	–	1.6	F‡	2.4	F‡	2.9	E‡	2.8	F‡	–	–	2.1	F‡
9069	[S III]	27.5	A‡	28.5	A‡	38.3	A‡	34.7	A‡	17.5	B‡	20.7	D‡	18.0	B‡
9229	P 9	–	–	3.8	F‡	4.0	D‡	–	–	4.0	D‡	–	–	3.0	C‡
9532	[S III]	77.8	A‡	81.5	A‡	90.4	A‡	75.8	A‡	20.7	B‡	45.7	D‡	37.7	B‡
	$E_{\beta-\alpha}$	0.25		0.27		0.13		0.27		0.01		0.26		$E_{\beta-\delta}$	−0.08⋆

† These lines sit in an absorption feature near 7200 Å.

‡ The fluxes are affected by telluric absorption. The extra uncertainty arising from this is not included here.

⋆ The H_α line was saturated. The Balmer-decrements H_γ/H_β and H_δ/H_β were used for the extinction correction. Given here is $E_{\beta-\delta}$.

part have their own set of 5 detectors (SW 1-5 and LW 1-5). The total spectrum is formed by adding the subspectra from each of the ten separate detectors in the LWS. For each source and for each of the ten detectors, six scans were obtained. The positions of the LWS beam on the sky are shown in Figs. 2 and 3.

The spectra were reduced with LWS Interactive Analysis (LIA) V8.7, starting at the SPD level. The reduction process involved six separate steps. In the first reduction step, the absolute response of the detectors is calibrated using the illuminator flashes bracketing every observation. Following this

Table 5. The ISO-SWS/LWS fluxes for the LMC objects N160A1, N160A2, N159-5, N157B, N4A, N11A, N83B and N79A. The first and second column give the wavelength and identification of the lines, respectively. The fluxes are given in 10^{-16} W m^{-2}. The flux uncertainties are coded as follows: A < 5%, 5% ≤ B < 10%, 10% ≤ C < 15%, 15% ≤ D < 20%, 20% ≤ E < 30%, F ≥ 30%.

λ (μm)	Identifier	N160A1		N160A2		N159-5		N157B		N4A		N11A		N83B		N79A	
		Flux	Err	Flux	Err	Flux	Err	Flux	Err	Flux	Err	Flux	Err	Flux	Err	Flux	Err
4.05	Brα	51.7	C	55.2	C	12.6	C	–	–	10.7	E	–	–	12.3	D	–	–
2.63	Brβ	24.0	B	28.4	B	5.98	C	3.65	C	10.8	B	–	–	6.53	B	–	–
7.46	Pfα	16.1	F	15.5	D	–	–	–	–	6.50	D	–	–	–	–	–	–
4.65	Pfβ	7.73	D	9.43	D	–	–	–	–	–	–	–	–	–	–	–	–
12.8	[Ne II]	112	E	124	E	51.0	E	28.5	E	41.1	E	18.9	E	18.9	E	–	–
15.6	[Ne III]	438	C	332	C	152	C	49.5	C	121	C	42.6	C	26.7	C	5.39	C
36.0	[Ne III]	70.6	F	55.9	F	17.9	F	7.35	F	20.4	F	6.22	F	4.92	F	–	–
18.7	[S III]	317	C	268	C	74.2	C	46.5	C	93.6	C	36.1	C	28.8	C	1.64/6.32	F/C
33.5	[S III]	643	F	491	F	204	F	116	F	212	F	60.3	F	52.2	F	24.8	F
10.5	[S IV]	289	C	194	C	56.7	C	11.7	C	75.9	C	23.3	C	18.1	C	2.49	C
34.8	[Si II]	111	F	120	F	80.5	F	44.0	F	32.5	F	14.4	F	15.1	F	14.2	F
6.98	[Ar II]	6.47	E	11.3	F	–	–	–	–	–	–	–	–	–	–	–	–
8.99	[Ar III]	70.3	C	76.2	C	19.9	C	8.72	D	25.8	C	11.6	C	10.7	C	–	–
25.99	[Fe II]	–	–	–	–	–	–	4.52	E	–	–	–	–	–	–	–	–
63.1	[O I]	890	B	890	B	540	B	106	B	182	B	270	B	153	C	63	C
145.5	[O I]	53	B	53	B	39	B	9	E	13	C	8.3	D	8.3	D	3.5	D
51.8	[O III]	3000	B	3000	B	1900	B	815	B	800	B	1140	B	130	C	151	C
88.3	[O III]	2700	B	2700	B	2250	B	1450	B	850	C	1710	B	140	C	275	C
25.91	[O IV]	–	–	–	–	–	–	5.09	D	–	–	–	–	–	–	–	–
121.8	[N II]	<22	⋆	<22	⋆	<23	⋆	<7	⋆	<7.5	⋆	<14	⋆	<6	⋆	<5	⋆
57.3	[N III]	275	B	275	B	187	B	77	C	67	C	133	C	<35	⋆	20	F
157.7	[C II]	595	B	595	B	560	B	170	B	160	B	270	B	156	B	81	B

⋆ 3 σ upper limit only.

is a correction for the drift in responsivity of every detector. The conversion from photocurrents (V s^{-1}) to flux units (W cm^{-2} μm^{-1}) is done in two steps: the relative response correction and the spectral element correction. The first of these two steps corrects for the wavelength-dependent responsivity of every separate detector, while the second step corrects for the size of its spectral element. Next, a dark current correction was applied. The last reduction steps were the wavelength calibration of the spectra and a correction for the line-of-sight velocity of the ISO spacecraft towards the object. For those objects for which the continuum was very weak (flux density lower than 300 Jy at 100 μm) the dark current subtraction was done a second time with extra care. This was done to prevent the baselines of the separate scans from becoming negative as a result of inaccurate dark current subtraction. The thus reduced spectra were further processed in ISAP, where they were manually deglitched, sigma clipped to remove the remaining outlying points and corrected for fringes. The up and down scan spectra were reduced separately and in combined form. The ten subspectra were then combined to give the total spectrum.

Table 6. The same as in Table 5 but then for the four pointings in 30 Doradus and the SMC sources N88A, N66 and N81.

λ (μm)	Identifier	30 Dor#1		30 Dor#2		30 Dor#3		30 Dor#4		N88A		N66		N81	
		Flux	Err	Flux	Err	Flux	Err	Flux	Err	Flux	Err	Flux	Err	Flux	Err
4.05	Brα	34.9	C	53.5	C	95.9	C	26.6	C	–	–	–	–	–	–
2.63	Brβ	16.0	B	27.0	B	45.8	B	12.7	C	8.45	C	1.83	F	5.60	D
7.46	Pfα	–	–	19.6	C	38.3	C	12.7	D	–	–	–	–	–	–
4.65	Pfβ	–	–	–	–	20.2	D	–	–	–	–	–	–	–	–
3.74	Pfγ	–	–	–	–	14.1	B	–	–	–	–	–	–	–	–
3.29	Pfδ	–	–	–	–	9.68	B	–	–	–	–	–	–	–	–
3.04	Pfϵ	–	–	–	–	8.73	C	–	–	–	–	–	–	–	–
2.87	Pfζ	–	–	–	–	4.92	C	–	–	–	–	–	–	–	–
12.8	[Ne II]	70.4	E	100	E	169	E	72.0	E	–	–	4.77	E	2.90	E
15.6	[Ne III]	371	C	689	C	1120	C	404	C	25.1	C	15.0	C	21.4	C
36.0	[Ne III]	109	F	123	F	194	F	87.1	F	6.75	F	–	–	1.60	F
18.7	[S III]	278	C	381	C	554	C	270	C	8.99	C	7.18	C	14.1	C
33.5	[S III]	785	F	921	F	1650	F	754	F	8.86	F	20.1	F	23.2	F
10.5	[S IV]	246	C	448	C	761	C	186	C	55.1	C	9.71	C	15.9	C
34.8	[Si II]	152	F	107	F	1440	F	116	F	13.1	F	–	–	6.20	F
6.98	[Ar II]	–	–	–	–	–	–	–	–	–	–	–	–	–	–
8.99	[Ar III]	49.3	C	71.9	C	146	C	45.7	C	8.07	D	3.55	E	3.90	C
21.8	[Ar III]	–	–	–	–	19.8	D	–	–	–	–	–	–	–	–
25.99	[Fe II]	–	–	–	–	–	–	–	–	–	–	–	–	–	–
63.1	[O I]	910	B	970	B	1140	B	830	B	86	B	105	D	37	B
145.5	[O I]	54	C	56	E	78	C	70	C	3	F	5	C	<2	–
51.8	[O III]	10000	B	12000	B	12200	B	8800	B	85	D	340	D	67	E
88.3	[O III]	10200	B	11700	B	11700	B	9400	B	22	F	590	C	74	E
25.91	[O IV]	–	–	–	–	–	–	–	–	–		–	–	–	–
121.8	[N II]	<26	⋆	<19	⋆	<25	⋆	<24	⋆	<4.5	⋆	<7	⋆	<2.5	⋆
57.3	[N III]	770	B	910	B	970	B	810	B	<32	⋆	<67	⋆	<38	⋆
157.7	[C II]	575	B	500	B	600	B	610	B	35	B	58	C	14	E

⋆ 3 σ Upper limit only.

The different subspectra were not corrected for detector-to-detector jumps in the baseline (stitching).

The line fluxes were measured in the same way as the SWS lines by fitting Gaussians (see Sect. 3.2.1). The approximation of the LWS lines by Gaussians introduces errors in the measured flux of less than 2.5% (Gry et al. 2000). The FWHM of the fitted Gaussians was held constant at 0.283 μm for the SW detectors and at 0.584 μm for the LW detectors. Extensive calibration of LWS has shown the FWHM of the lines to be constant for both sets of detectors (Gry et al. 2000). The fluxes were measured in the separate up and down scans and in the combined spectra. The fluxes from the combined up and down scans are given in Tables 5 and 6. For lines of which the flux was less than three times the noise level only an upper limit is given. No extinction correction has been applied to the LWS fluxes (see Sect. 3.2.1). Sources of uncertainty in the line fluxes include noise, differences between the fluxes measured in the up and down scan and the uncertainty in the absolute flux calibration. The uncertainty due to noise was determined from line-fit residuals. The main source of error is the uncertainty in the flux calibration. For strong sources, this uncertainty is in the order of 10%. For weak sources or for sources with a complex morphology, however, this uncertainty can be as high as

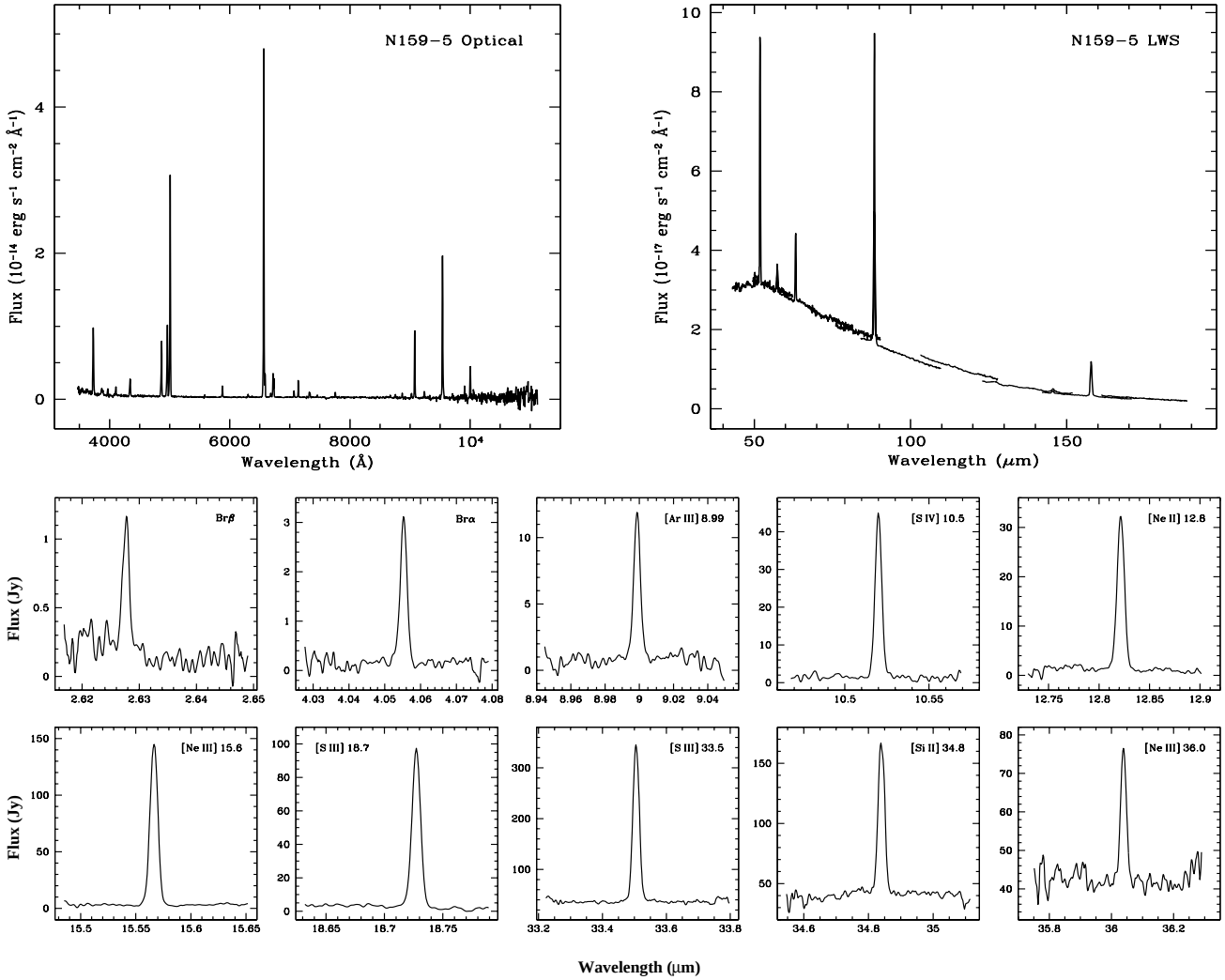

Fig. 4. The optical and infrared spectra from N159-5. The top part shows the optical (*left*) and LWS (*right*) spectra, the bottom part the SWS line scans.

30%. These numbers apply to every detector except the detectors SW1 and LW2 for which the calibration is less clear.

3.3. The spectra

Examples of the spectra are given for the LMC objects N159-5 (Fig. 4) and N83B (Fig. 5). Shown in these Figures are the optical spectrum (upper left panel), the LWS spectrum (upper right panel) and the separate SWS line scans (lower panel). Also shown in Fig. 6 are the combined optical and infrared spectra of 30 Doradus#1. These spectra serve as an example of the general quality of our data, where the spectra of LMC-N83B represent the lower end of the quality scale. It is worth noting that the spectral coverage of the 30 Doradus#1 spectra is almost continuous and spans three decades.

4. Discussion

The line fluxes presented in this paper suffer from a number of extra uncertainties, which break down into two groups. One has to do with the extinction correction of the fluxes, the other with the problem of different instrumental beams and the size of the sample objects. The problems connected with the extinction correction are the most important for the optical line fluxes. For the infrared data the extinction is negligible.

4.1. Extinction correction

The optical spectra given in this paper are all driftscan spectra. The surface integrated spectra make the comparison between the optical and infrared fluxes easier, but they also present a problem for the extinction correction of the line fluxes. This has to do with the non-uniform nature of the extinction across an object, which is especially a problem in very complex environments like star-forming regions, where the extinction can change drastically from one point to another. A good example in this respect is the SMC object N88A. In a recent paper, Heydari-Malayeri et al. (1999a) showed that even within an object with such a small angular size (3.″5), the Hα/Hβ intensity ratio can change drastically within a few arcseconds. This general "patchiness" of the extinction across the face of an object, however, is smeared in a driftscan spectrum. The resulting

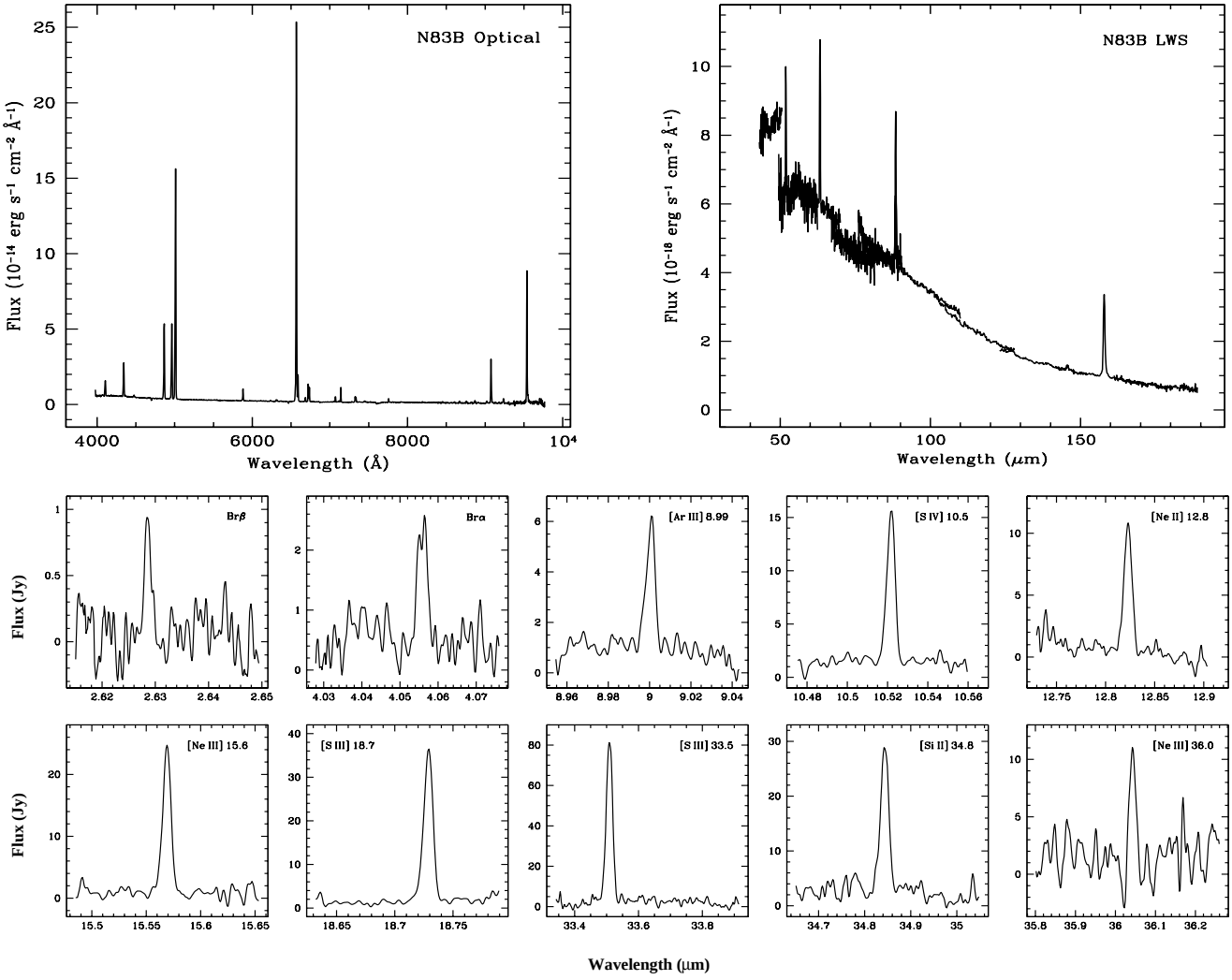

Fig. 5. The optical and infrared spectra from N83B. The top part shows the optical (*left*) and LWS (*right*) spectra, the bottom part the SWS line scans.

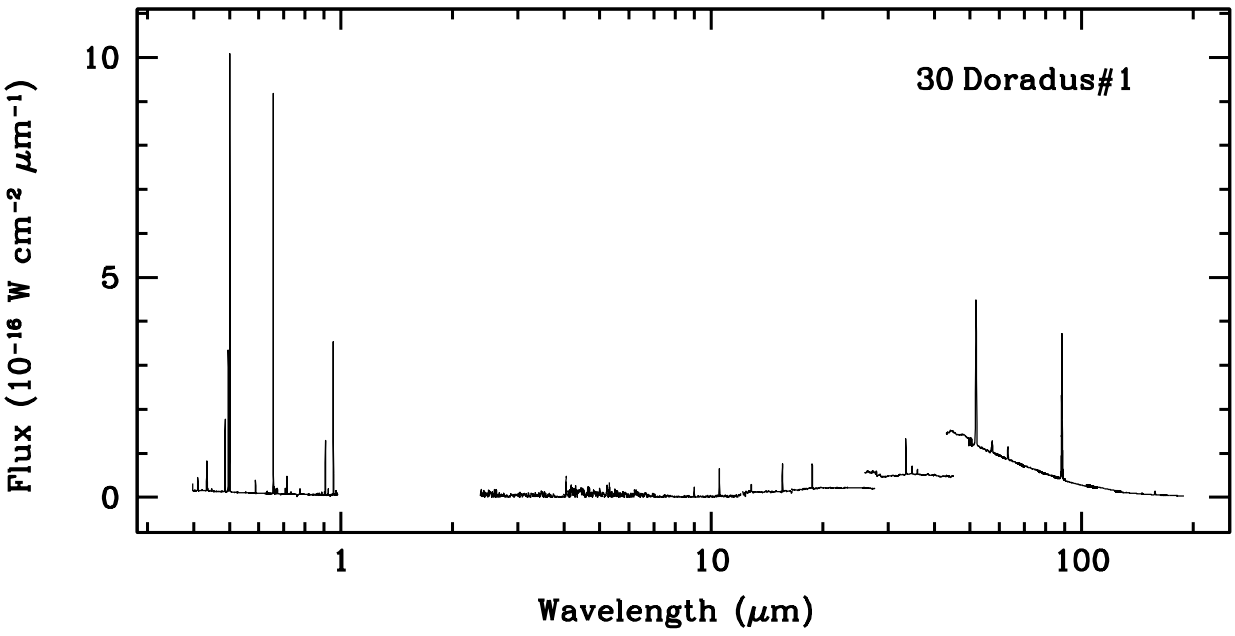

Fig. 6. The optical and infrared spectra from 30 Doradus#1. Note the almost continous spectral coverage over three decades.

Balmer-decrements on which the extinction correction is based are therefore a complicated "weighted average" that reflects the variation in extinction properties encountered across the area scanned.

Related to the problem of the non-uniformity of the extinction, is the issue of what extinction curve to apply. In this work, a general extinction curve was used for the reddening correction of the optical data. The assumption made in the correction applied was that all the extinction can be ascribed to foreground extinction. Furthermore, an implicit assumption made is that the properties of the absorbing matter are the same everywhere, which is reflected in the "unchangeable" shape of the extinction curve adopted.

The assumptions about the origin of the extinction and the shape of the extinction curve are invalidated when extinction within the source itself also becomes important. The absorption and scattering properties of the matter inside the source can be different from those of the matter external to the source, this as a result of the drastically different environment within the source. In this case, the shape of the extinction curve will be modified. A situation where this can become important is when dust is mixed with the emitting gas of an object. Objects in the sample which are known to have internal dust are SMC-N88A (Kurt et al. 1999), and the LMC objects N159-5 and N160A1. Furthermore, any dust mixed with the ionized gas can decrease the Balmer-decrements found in the spectrum (Mathis 1983).

Both of the uncertainties described here will have repercussions for the line fluxes given. The smearing of the extinction in a driftscan spectrum will lead to an underestimate of the correction to apply, while the unknown variations in the shape of the extinction curve will give unknown wavelength dependent variations in the total extinction correction. One should bear in mind, however, that everything said in this Section will only affect the fluxes which have actually been corrected for extinction (i.e. the optical fluxes). The same problems also affect the extinction correction of the infrared lines but no correction has been applied here.

4.2. Telluric absorption

An additional problem affecting the optical line fluxes is the absorption from water in the atmosphere. The line fluxes redwards from 8000 Å are affected by it, and it is especially important for the [S III] 9068 Å and [S III] 9532 Å lines. The presence of this absorption is clearly visible in the standard star spectra and in some of the object spectra. The amount of telluric absorption is difficult to asses, because it depends critically on the degree of overlap between the telluric and the spectral lines. Also, given the low spectral resolution of our spectra of about 4 Å, the narrow telluric lines are blended and only a broad absorption feature is seen. We can, therefore, only give a rough estimate of the extra uncertainty on our line fluxes introduced by this absorption, and did not attempt to actually correct the fluxes for this. We thereby focussed our attention exclusively on the crucial [S III] lines.

To get a rough idea of the magnitude of the telluric extinction, the depths of the absorption features seen in the standard star exposures were measured. The absolute values of the amount of absorption themselves were not very useful because of the changes in the atmospheric conditions from night to night, but it was possible to establish a ratio for the absorption near [S III] 9068 Å and near [S III] 9532 Å. It turned out that the absorption at [S III] 9532 Å was in all cases roughly three times larger than at [S III] 9068 Å. The absorption near [S III] 9068 Å was at most 0.1 mag.

The actual estimation of the extra uncertainty on our line fluxes involved the use of the theoretical line flux ratio of the two [S III] lines. The theoretical ratio [S III] 9532/[S III] 9068 is 2.44, the ratio of the transition probabilities. The observed [S III] 9532/[S III] 9068 ratio was compared with the theoretical one, and the correction factor needed to arrive at the theoretical ratio was derived. The deviation of the observed ratio from the theoretical one is (most likely) due to absorption in *both* the [S III] lines. The correction factor described above, therefore, depends on the effect of the (unknown) absorption on *both* the lines. Taking this dependency into account, we derived a matrix of correction factors for the [S III] 9532 Å and the [S III] 9068 Å line flux from which the uncertainty was estimated.

Taking into account the relative difference in absorption near the two lines and the fact that the [S III] 9068 Å line appeared more reliable than the [S III] 9532 Å line, the investigation of the parameter space of correction factors led us to estimate that there is an extra uncertainty in the line fluxes of up to 20%. This uncertainty is not included in the error given for these lines in Tables 3 and 4.

4.3. Apertures and beams

An important issue, concerning the infrared line fluxes, is the question whether or not the sample objects are pointlike or extended compared to the ISO-SWS/LWS apertures. Any deviation of the source morphology from a perfect point source gives rise to a set of inter-related problems, resulting from the multitude of apertures and beams involved with the ISO spectrometers.

The total spectral coverage of the ISO spectrometers is subdivided into several subregions or bands, and all these different parts of the spectrum are observed through different apertures. The four rectangular ISO-SWS apertures through which the different spectral ranges are observed cover an area on the sky of 14″× 20″ (2.38–12.0 μm), 14″× 27″ (12.0–27.5 μm), 20″× 27″ (27.5–29.0 μm) and 20″× 33″ (29.0–45.2 μm), respectively. The circular ISO-LWS aperture is about 80″ in diameter. The result of the subdivision is that, depending on wavelength, different spatial areas of a sample object are observed.

All these apertures also have their own wavelength dependent throughput or beam profile. The beam profiles drop off sharply when one moves away from the centre of the aperture, which can lead to a significant loss of flux. In the ideal cases of an infinitely extended and homogeneous object or a point source, a correction for the loss of flux can be made. However, for a realistic object, where the resultant flux is a convolution of the beam profile and the source morphology, it is very difficult to make such corrections.

With these two facts in mind, it will also be clear that not only the source morphology is of importance but also the position of the source in the aperture. If an object is located at the edge of one or more of the apertures, the flux losses can be severe. These losses can hardly be traced or restored. It is therefore important that the intended target is in the centre of the aperture. Objects in our sample not satisfying this requirement are SMC-N81 and SMC-N88A, which are lying near the edge of the LWS aperture (see Fig. 3, center).

In this respect, a comment must be made about the pointings of the two ISO spectrometers for the sample sources. As can be seen in Table 1 and even more clearly in Figs. 2 and 3, there are sometimes considerable differences between the pointings of SWS and LWS, despite the fact that the pointings were meant to be exactly the same. The most serious cases are LMC-N11A (Fig. 2, lower left), where LWS was actually pointed at LMC-N11B, and the object LMC-N79A which falls outside the SWS beam completely (Fig. 3, upper left). In many cases, though, the pointing differences are only slight.

The problems described above raise the issue of flux (in)compatibility. This is a serious handicap for the analysis done with the line fluxes, which is primarily based on flux ratios of different fine-structure and recombination lines. The impact of the flux incompatibility on the analysis depends on the lines used. For lines observed through the same aperture, where the degree of incompatibility is likely to be small (e.g. Brβ and [S IV] 10.5 μm), the result will be more reliable than for lines observed through different apertures (e.g. [S III] 18.7 μm and [S III] 33.5 μm). It is obvious that any analysis based on the infrared line fluxes should be done with these caveats in mind.

5. Summary

As part of an ISO Guaranteed Time Program on H II regions in Local Group Galaxies a sample of Magellanic Cloud H II regions has been observed with the spectrometers onboard ISO. Complementary to the infrared data is a large set of optical spectra. Aim of the project is to give a new and improved analysis of the physical structure of the sample H II regions by combining as much spectral data as possible.

In this first of a set of papers, the sample objects and the data set are presented. An account is given of the reduction of the data and a discussion about the reliability of the line fluxes is presented. In this discussion, attention has been paid to problems regarding extinction and to problems generated by the SWS/LWS instruments themselves. The analysis based on this data set will be given in different papers. The results on the large-scale temperature stratification, the elemental abundances and the ionization structure of the sample H II regions will be presented in Vermeij & Van der Hulst (2002). The analysis of the photodissociation regions based on the LWS lines will be given in Damour et al. (in prep.).

Acknowledgements. We would like to thank the referee for his constructive criticism and comments which helped to improve the paper. The ISO Spectral Analysis Package (ISAP) is a joint development by the LWS and SWS Instrument Teams and Data Centers. Contributing institutes are CESR, IAS, IPAC, MPE, RAL and SRON. IA^3 is a joint development of the SWS consortium. Contributing institutes are SRON, MPE, KUL and the ESA Astrophysics Division. LIA is a joint development of the LWS consortium. Contributing institutes are DRAL, CESR and the ESA Astrophysics Division.

References

Baker, J. G., & Menzel, D. H. 1938, ApJ, 88, 52
Bothun, G. D., & Thompson, I. B. 1988, AJ, 96, 877
Clegg, P. E., Ade, P. A. R., Armand, C., et al. 1996, A&A, 315, L38
Contursi, A., Lequeux, J., Hanus, M., et al. 1998, A&A, 336, 662
Contursi, A., Lequeux, J., Cesarsky, D., et al. 2000, A&A, 362, 310
Chu, Y.-H., & Kennicutt Jr, R. C. 1994, ApJ, 425, 720
Danziger, I. J., Goss, W. M., Murdin, P., Clark, D. H., & Boksenberg, A. 1981, MNRAS, 195, 33
Dickel, J. R., Milne, D. K., Kennicutt, R. C., Chu, Y.-H., & Schommer, R. A. 1994, AJ, 107, 1067
Dufour, R. J., & Harlow, W. V. 1977, ApJ, 216, 706
Feast, M. W. 1999, PASP, 111, 775
de Graauw, Th., Haser, L. N., Beintema, D. A., et al. 1996, A&A, 315, L49
Garnett, D. R. 1989, ApJ, 345, 282
Grandi, S. A., & Hawley, S. A. 1978, PASP, 90, 125
Gry, C., et al. 2000, LWS handbook SAI/99-077/Dc V1.1
Henize, K. G. 1956, ApJS, 2, 315
Heydari-Malayeri, M., & Testor, G. 1983, A&A, 118, 116
Heydari-Malayeri, M., & Testor, G. 1985, A&A, 144, 98
Heydari-Malayeri, M., Le Bertre, T., & Magain, P. 1988, A&A, 195, 230
Heydari-Malayeri, M., Van Drom, E., & Leisy, P. 1990, A&A, 240, 481
Heydari-Malayeri, M., & Lecavalier des Etangs, A. 1994, A&A, 291, 960
Heydari-Malayeri, M., Charmandaris, V., Deharveng, L., Rosa, M. R., & Zinnecker, H. 1999a, A&A, 347, 841
Heydari-Malayeri, M., Rosa, M. R., Charmandaris, V., Deharveng, L., & Zinnecker, H. 1999b, A&A, 352, 665
Heydari-Malayeri, M., Rosa, M. R., Zinnecker, H., Deharveng, L., & Charmandaris, V. 1999c, A&A, 344, 848
Heydari-Malayeri, M., Charmandaris, V., Deharveng, L., et al. 2001a, A&A, 372, 495
Heydari-Malayeri, M., Charmandaris, V., Deharveng, L., et al. 2001b, A&A, 372, 527
Heydari-Malayeri, M., Charmandaris, V., Deharveng, L., et al. 2002, A&A, 381, 941
Howarth, I. D. 1983, MNRAS, 203, 301
Hunter, D. A., Shaya, E. J., Holtzman, J. A., & Light, R. M. 1995, ApJ, 448, 179
Johansson, L. E. B., Greve, A., Booth, R. S., et al. 1998, A&A, 331, 857
Kennicutt Jr, R. C., Bomans, D. J., Bothun, G. D. & Thompson, I. B. 1995, AJ, 109, 594
Kennicutt Jr, R. C, Bresolin, F., French, H., & Martin, P. 2000, ApJ, 537, 589
Kessler, M. F., Steinz, J. A., Anderegg, M. E., et al. 1996, A&A, 315, 27
Kovács, G. 2000, A&A, 360, L1
Kurt, C. M., Dufour, R. J., Garnett, D. R., et al. 1999, ApJ, 518, 246
Long, K. S., & Helfand, D. J. 1979, ApJ, 234, L77
Lucke, P. B., & Hodge, P. W. 1970, AJ, 75, 171
Le Marne, A. E. 1968, MNRAS, 139, 461

Marshall, F. E., Gotthelf, E. V., Zhang, W., Middleditch, J., & Wang, Q. D. 1998, ApJ, 499, L179
Massey, P., & Hunter, D. A. 1998, ApJ, 493, 180
Massey, P., Parker, J. W., & Garmany, C. 1989, AJ, 98, 1305
Mathis, J. S. 1983, ApJ, 267, 119
Mathis, J. S., Chu, Y.-H., & Peterson, D. E. 1985, ApJ, 292, 155
Mathis, J. S., & Rosa, M. R. 1991, A&A, 245, 625
Mills, B. Y., Turtle, A. J., & Watkinson, A. 1978, MNRAS, 185, 263
Natta, A., Panagia, N., & Preite-Martinez, A. 1980, ApJ, 242, 596
Oke, J. B. 1974, ApJS, 27, 21
Pagel, B. E. J., Edmunds, M. G., Fosbury, R. A. E., & Webster, B. L. 1978, MNRAS, 184, 569
Parker, J. Wm. 1993, AJ, 106, 560
Parker, J. Wm., & Garmany, C. D. 1993, AJ, 106, 1471
Peimbert, M. 1967, ApJ, 150, 825
Peimbert, M., & Costero, R. 1969, Bol. Obs. Tonantzintla y Tacubaya, 5, 3
Rosa, M., & Mathis, J. S. 1987, ApJ, 317, 163
Rosado, M., Laval, A., Le Coarer, E., et al. 1996, A&A, 308, 588
Rubio, M., Contursi, A., Lequeux, et al. 2000, A&A, 359, 1139
Taisheng, Y., Turtle, A. J., & Kennicutt Jr, R. C. 1991, MNRAS, 249, 722
Schild, H., & Testor, G. 1992, A&AS, 92, 729
Scowen, P. A., Hester, J. J., Sankrit, R., et al. 1998, AJ, 116, 163
Storey, P. J., & Hummer, D. G. 1995, MNRAS, 272, 41
Testor, G., & Pakull, M. 1985, A&A, 145, 170
Van Loon, J. Th., & Zijlstra, A. A. 2001, ApJ, 547, L61
Vermeij, R., & Van der Hulst, J. M. 2002, A&A, submitted
Vilchez, J. M., & Pagel, B. E. J. 1988, MNRAS, 231, 257
Walborn, N. R., & Blades, J. C. 1997, ApJS, 112, 457
Wang, Q. D. 1999, ApJ, 510, L139
Whiteoak, J. B., Wellington, K. J., Jauncey, D. L. et al. 1983, MNRAS, 205, 275